Research Article Vol. 31, No. 11 / 22 May 2023 / *Optics Express* 17964

Optics EXPRESS

Quantitative laser–matter interaction: a 3D study of UV-fs-laser ablation on single crystalline Ru(0001)

VALENTINE GRIMAUDO,[1] DIEGO MONSERRAT LOPEZ,[2] GIULIA PRONE,[2] THOMAS LÜTHI,[3] ALEXANDER FLISCH,[3] ALENA CEDEÑO LÓPEZ,[4] VITALI GROZOVSKI,[4] MAREK TULEJ,[1] ANDREAS RIEDO,[1,*] ROBERT ZBORAY,[3] EMANUEL LÖRTSCHER,[2] PETER BROEKMANN,[4] AND PETER WURZ[1]

[1] *Physics Institute, Space Research and Planetary Sciences, University of Bern, Sidlerstrasse 5, CH-3012 Bern, Switzerland*
[2] *IBM Research Europe – Zurich, Science of Quantum and Information Technology Department, Säumerstrasse 4, CH-8803 Rüschlikon, Switzerland*
[3] *Center for X-ray Analytics, EMPA Material Science and Technology, Überlandstrasse 129, CH-8600 Dübendorf, Switzerland*
[4] *Department of Chemistry, Biochemistry and Pharmaceutical Sciences, University of Bern, Freiestrasse 3, CH-3012 Bern, Switzerland*
[*] *andreas.riedo@unibe.ch*

Abstract: Laser ablation is nowadays an extensively applied technology to probe the chemical composition of solid materials. It allows for precise targeting of micrometer objects on and in samples, and enables chemical depth profiling with nanometer resolution. An in-depth understanding of the 3D geometry of the ablation craters is crucial for precise calibration of the depth scale in chemical depth profiles. Herein we present a comprehensive study on laser ablation processes using a Gaussian-shaped UV-femtosecond irradiation source and present how the combination of three different imaging methods (scanning electron microscopy, interferometric microscopy, and X-ray computed tomography) can provide accurate information on the crater's shapes. Crater analysis by applying X-ray computed tomography is of considerable interest because it allows the imaging of an array of craters in one step with sub-µm accuracy and is not limited to the aspect ratio of the crater. X-ray computed tomography thereby complements the analysis of laser ablation craters. The study investigates the effect of laser pulse energy and laser burst count on a single crystal Ru(0001) sample. Single crystals ensure that there is no dependence on the grain orientations during the laser ablation process. An array of 156 craters of different dimensions ranging from <20 nm to ~40 µm in depth were created. For each individually applied laser pulse, we measured the number of ions generated in the ablation plume with our laser ablation ionization mass spectrometer. We show to which extent the combination of these four techniques reveals valuable information on the ablation threshold, the ablation rate, and the limiting ablation depth. The latter is expected to be a consequence of decreasing irradiance upon increasing crater surface area. The ion signal generated was found to be proportional to the volume ablated up to the certain depth, which enables in-situ depth calibration during the measurement.

1. Introduction

Since the development of the Q-switched pulsed laser beams [1], lasers have become important tools for the analysis of solid materials as an efficient ablation or as molecular or atomic ion

#485713 https://doi.org/10.1364/OE.485713
Journal © 2023 Received 7 Mar 2023; revised 28 Apr 2023; accepted 28 Apr 2023; published 12 May 2023

source for analytical instruments [2]. Such ion sources can easily be coupled to mass analyzers to study the chemical composition of the analyte [3,4]. Various analytical techniques such as laser ablation/desorption mass spectrometry (e.g., LAMMA) [5], matrix-assisted laser desorption ionization (MALDI) mass spectrometry [6], laser ablation inductively coupled mass spectrometry (LA-ICP-MS) [7,8], laser induced breakdown spectroscopy (LIBS) [9,10], or resonance ionization mass spectrometry (RIMS) [11] employ lasers of various wavelengths, pulse durations and energies or repetition rates. Nowadays laser ablation ion sources offer also new capabilities for chemical surface imaging and high-resolution depth profiling. Laser beams can be focused to well-controlled micrometer spots and below, which allows for microscopic sampling of inhomogeneous samples [12–16]. The need in the microtechnology community to apply lasers as a microscopic slicing instrument significantly contributed to a better understanding of laser–matter interaction and led to an increase of the irradiation power and ablation precision [17]. The introduction of laser systems with pulse widths below picosecond duration was a breakthrough for analytics. High-intensity pulses (at the level TW cm^{-2}) allowed for spatially uniform ablation and ionization of materials with minimal peripheral damages. This again has led to higher spatial resolution in the vertical and lateral direction and to the stoichiometric determination of the element composition of the sample of interest [18–20]. To date, femtosecond laser pulse irradiation is widely applied in LA-ICP-MS [21], LIBS [22] and laser ablation ionization mass spectrometry (LIMS) [23] for depth profiling of the chemical composition, e.g. along vertically layered stacks. For accurate spatial assignment of the chemical information recorded, it is necessary to understand how the laser irradiation geometrically and temporally forms the crater shape and to which extent every single pulse contributes to the removal of the material. Particularly when probing at the smallest possible spatial scale, the detailed understanding of the crater formation and evolution requires a three-dimensional evaluation of the generated crater. In the last two decades, laser-induced crater morphology was investigated by various techniques such as atomic force microscopy (AFM) [24], white-light interferometry [25], or confocal microscopy [26]. However, these direct metrology techniques are limited to craters with relatively low aspect ratios (depth-to-diameter) or overall depths. New methods were developed to overcome these constraints enabling investigations of the ablation behavior in deeper craters or with higher aspect ratios. For instance, Borisov et al. [27] analyzed laser ablation craters formed at the junction of two polished pieces of the same glass material that were mated and secured by tape. Afterward, the craters' cross-sections along the junction were analyzed with an electron microscope. Another method for the analysis of the crater shape is the trans-illumination of semiconductors such as Si, which have the property to become transparent to illumination with light of a frequency below or at the band edge of the ablated substrate. The transmitted light is then detected in situ during the ablation procedure with a standard CCD camera [28,29]. Two novel procedures that enable the analysis of entire laser ablation crater arrays in a short time were developed by us. The first method is based on the anisotropic etching of Si for cross-sectioning of the craters via multiple cycles of Si etching and passivation (the so-called Bosch-process). A lithographical mask that is placed on the surface of the substrate after the ablation process is applied to selectively etch Si to create cross-sectional cuts along the crater's axis. Note, this approach is material-specific and only applicable to Si. The second approach is based on the fabrication of a three-dimensional mold of the laser ablation craters through curing of a polymer that is poured into the craters and then released [30–32]. Both methods provide detailed morphological information of the entire ablation crater. In particular, the second approach is useful to investigate ablation properties, because it is applicable to a wide range of different material classes, fully volumetric in nature and non-invasive, which allows for multiple molds of the same craters. Previous studies used scanning electron microscopy (SEM) with a tilted sample stage to investigate the crater depth via the height of the molds. The average ablation rate (AAR) can be obtained with this method, but the procedure requires the sample to be rotated to capture the full 3D information from 2D

SEM measurements. To enable a volumetric, automated and scalable determination of the laser ablation craters, we recently extended the PDMS molding by the analysis of the crater's negative by X-ray computed tomography (CT) [33]. This novel approach is accurate for sub-micrometer structures and enables all relevant parameters to be extracted from the created digital surface topography. X-ray CT has already been used in the past for the direct characterization of enamel and dentine laser ablation craters with an Er:YAG laser and craters formed in an Al substrate and a rock sample with nanosecond laser irradiation [34,35].

In this study the accurate quantification of the entire crater volume is performed by standard methods and extended by the novel X-ray CT method. Contrary to those studies based on direct measurements of the craters, in this work we analyze the molded features of the craters with the X-ray CT. Analyzing the polymer instead of the original sample allows the replication of a subset of the original sample to maximize the spatial resolution in CT to below micrometer, since the resolution is inversely proportional to the distance of the sample to the X-ray source of the CT. Furthermore, polymers need less penetration power compared to metals that allows lab-sized (instead of synchrotron) X-ray sources and a smaller focal spot size of the X-ray source to be used. To obtain higher spatial resolution is particularly important in our case, because of the small dimensions of the craters (<10 µm). To create them, we used a UV-femtosecond irradiation source for the ablation of the material. To study in detail the ablation behavior a wide range of pulse energies, starting from below the ablation threshold were applied. Also, the number of laser burst counts was varied over wide range. Laser ablation craters of a different size with diameters down to ~3 µm, and depths ranging from tens of nm up to ~40 µm, were generated this way. These dimensions correspond to the typically depth profiling experiments our LIMS instrument is conducting. The X-ray CT study was complemented by interferometric microscopy and SEM analysis, in particular for those crater depths below the resolving power of the X-ray CT instrument applied. Furthermore, the ion signal measured with the mass spectrometer of the LIMS instrument is correlated to the amount of removed material.

Understanding how the ion signals acquired correlates to the crater shapes generated allows for predictions of the ablation process. The amount of material removed per single laser pulse depends on the applied laser parameters, e.g., temporal pulse width τ, wavelength, pulse energy, and size of the irradiated surface area. In turn, the irradiated surface area depends on both the beam waist and the characteristic distribution of the energy normal to the propagation axis of the laser beam. Irradiation with a Gaussian spatial distribution of the energy fluence induces craters with conical shapes, as the center of the irradiated surface encounters larger energy than the edges. This leads to a continuous enlargement of the crater surface, assuming a homogeneously distributed pulse within the crater. Hence, each laser pulse will encounter a different surface area, which affects the irradiance (laser power/surface area) and the ablation rate.

2. Materials and methods

2.1. Sample

The extensive laser ablation study was performed on a cylindrical-shaped (5 mm Ø × 3 mm) Ru(0001) single crystal (MaTecK, Germany). Single crystals ensure that there is no dependence of the ablation process on the grain orientations, the grain size, interfaces between grains and other sample inhomogeneities. The analysis of the crater evolution during laser ablation on a single crystal sample with surface roughness at nm level constitutes an ideal platform for testing different laser ablation measurement parameters.

2.2. Laser source

In this study, only the essential components and parameters relevant for the study are highlighted. A detailed description of the LIMS instrument setup is given in previous publications [20,36–38].

The laser used as ion source in this study was a chirped pulse amplified (CPA) (Clark-MXR Inc., Dexter, MI, USA) laser, which generates a fundamental wavelength of 775 nm with ~190 fs pulse widths. Harmonic generators (Storc, Clark-MXR Inc.) convert the fundamental beam to a wavelength of 258 nm. A beam expander (Eksma Optics, Vilnius, Lithuania) enlarges the beam from a diameter of about 2–3 mm to about 30 mm. A periscope consisting of dielectric mirrors is used to redirect the beam from the beam expander to the entrance window of the vacuum chamber, and subsequently to the sample and mass analyzer, both of which are situated in this chamber. A doublet-lens system with a focal length of 250 mm, situated directly above the mass analyzer inside the vacuum chamber, is used to focus the beam along the central axis through the mass analyzer towards the sample surface, where each laser pulse ablates a distinct layer of material.

The sample was mounted on an x-y-z translation stage (with a positioning accuracy at the micrometer level) with the irradiated surface normal to the propagation axis of the laser beam and positioned in the focal plane of the laser. The focal plane is typically situated directly below the entrance ion optics of the mass analyzer (~0.5 mm), which was verified by monitoring the signal intensity and crater size with low pulse energies near the ablation threshold. The focal plane was identified as the position where the largest ion signal was observed.

In this configuration, the induced ablation plume is normal to the sample surface and a large faction of the plume expands into the ion optics of the mass analyzer. The ablated material was measured directly without using any carrier gas or additional ionization source (e.g., ICP).

2.3. Laser ablation

The study involved the application of different numbers of applied laser pulses (1, 2, 5, 10, 20, 50, 100, 200, 500, 1,000, 2,000, 5,000 and 10,000), so called bursts, at various laser pulse energies (0.02, 0.04, 0.09, 0.11, 0.14, 0.18, 0.22, 0.29, 0.37, 0.45, 0.58, and 0.72 µJ), each applied on a fresh sample location at a laser pulse repetition rate of 1 kHz. Before and after each complete measurement run the actually applied pulse energy was recorded with a J-10 MB-LE sensor (Coherent, Santa Clara, CA, USA) by measuring an average of 10,000 pulses in front of the beam expander. The measured pulse energies were then corrected for transmission losses (from the point of measurement towards the sample surface). Five repetitions were performed for each unique combination of applied number of pulses and pulse energy, resulting in a total crater array of 780 craters (13 burst counts x 12 pulse energies x 5 repetitions) (see Fig. 1).

The pitch between the laser burst counts and the repetitions was set to 50 µm, while the pitch between measurement runs involving different pulse energies was set to 100 µm, resulting in a total sampled area of 0.6×3.2 mm^2. All measurements were performed in vacuum at a base pressure of ~10^{-7} mbar.

2.4. Mass spectrometry

The LIMS instrument consists of a miniature reflectron-type time-of-flight mass spectrometer. The ion optical settings at the entrance extract only positively charged species. The detector system is located just above the entrance of the ion optics and consists of two centrosymmetric microchannel plates (MCPs) arranged in chevron configuration, and of four anode rings that can be operated to record at different gain levels [36,37]. The design of the detector allows the laser beam to be aligned co-linearly with the ion trajectories, which range from the ion source to the ion mirror (reflectron), and from the ion mirror back to the detector system. The design of the ion extraction (direct entrance of the ablation plume), the sensitivity of the detector, and the fast read-out acquisition system allow to measure the ions of the ablated material from each individually applied laser pulse.

A high-speed ADC card (U5303A, Acqiris SA, Geneva, Switzerland, two channels per card) is used to record the signal captured on the anodes at up to 3.2 GS/s with a 12-bit dynamic range

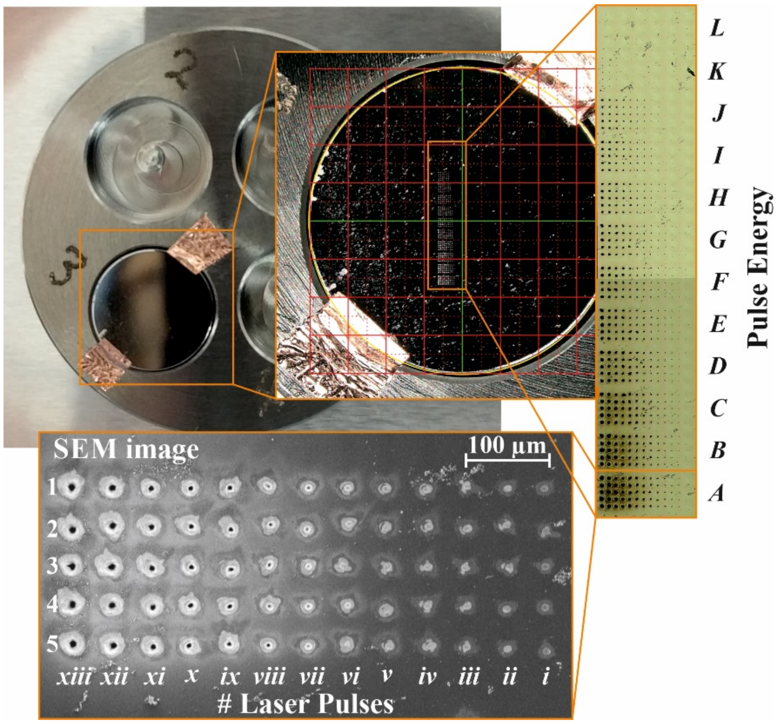

Fig. 1. Images of the sample and the produced craters at increasing spatial resolution. The series of measurement consists of 12 different laser pulse energies (A-L: 0.72 - 0.02 µJ) and 13 different laser burst counts (i–xiii: 1 – 10,000). For statistical reasons, each measurement set was repeated five times.

per laser shot. In the current study, the generated ions were recorded by one channel with a vertical 1 V full-scale range. For each laser pulse a TOF spectrum was recorded, at a 1 kHz laser pulse repetition rate (i.e., a burst count of 10,000 pulses generated 10,000 spectra recorded in ~10 s). In-house written software packages were used for the automation of the entire instrument (laser system, data acquisition, and sample stage) as well as the data processing following the measurements [39].

2.5. Scanning electron microscopy (SEM)

SEM micrographs were recorded with a Zeiss Gemini SEM (Zeiss, Germany) at an accelerating voltage of 10 kV and a working distance of 8.5 mm. The PDMS was coated with 5-7 nm of Au to prevent electrical charging by allowing the electrons to drain via the conductive surface coating. The analysis of the PDMS cast (see sections below) was done under a tilt-angle of 70°.

2.6. Interferometry micrographs (IM)

White light Interferometry Micrographs (IM) were recorded with a Contour GT interferometer (Bruker, USA) in vertical scanning interferometry (VSI) mode at a magnification of 40x. Analysis of the micrographs was performed with the Bruker Vision64 MapTM software and the Gwyddion [40] software tool. In this configuration the investigated features can be imaged with approx. 10–30 nm, and approx. 0.24 µm vertical and lateral resolution, respectively. Note, the presented line scans of the investigated ablation craters derived from interferometry analysis are conducted in one direction of the ablation crater only (not an average over e.g., 360 degrees of an entire crater), within a single frame of orientation. The induced laser ablation craters showed a minor elliptic geometry (almost not visible), and the profile corresponds to the larger axis of the ablation crater (additional information in Section 3.3).

2.7. PDMS casting of laser-induced craters

A polydimethylsiloxane (PDMS) based casting approach was used to obtain a three-dimensional 'negative' of the laser ablation craters. The PDMS casting allows to replicate 3D spatial structures at micro- and nanometer dimension with an accuracy at the sub-10 nm level. A detailed explanation of the casting procedure is provided in earlier publications [30].

To ensure the highest possible resolution of the subsequent CT-measurement (see the following section and Monserrat et al. [33]), the PDMS cast was performed in a pre-defined mold with 1.5 mm diameter. The size of the mold covered the entire measurement run (complete array of laser burst counts) of five different pulse energies (0.29, 0.37, 0.45, 0.58, and 0.7 µJ). Therefore, the 3D analysis by X-ray CT in this contribution is constrained to these five pulse energies. In Fig. 2 the schematic illustration of laser ablation, PDMS casting, and X-ray CT imaging is shown.

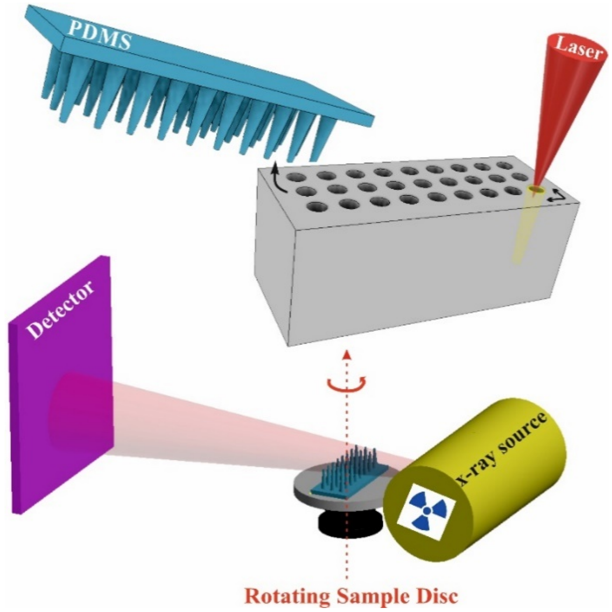

Fig. 2. Schematic illustrating the PDMS casting after crater formation by laser ablation, followed by X-ray CT measurement of the PDMS mold.

2.8. X-ray computed tomography (CT)

The X-ray CT instrument applied in this study is described in full detail in our previous publication [33]. The instrumentation used allows for imaging of small scale spatial features with an accuracy of better than 500 nm. Previous measurements on bottom-up fabricated test specimen, having a similar shape and dimension as the here investigated laser ablation craters showed an accuracy of 300–500 nm [33].

We used a RX Solutions EasyTom XL Ultra 230-160 with a Hamamatsu L10711 160 kV microfocus X-ray tube with LaB_6 cathode (limiting the voltage to 100 kV) and a 1 µm thick tungsten target, covered with 0.5 mm diamond for heat dissipation and additional water-cooling of the tube head. The detector used was a Varian flat panel 2,520 array, 1,920 × 1,536 pixels with

127 µm pitch with columnar grown CsI as scintillating material. With a source-object distance of 3.0 mm and a source-detector distance of 417 mm, the resulting geometrical magnification was roughly 140. The used acceleration voltage was 60 kV with a nominal current of 160 µA and a resulting target current of 5.5 µA. The number of projections was 1,440 over 360° rotation of the sample. The scan time was roughly 5 h. The heat transfer to and the radiation dose on the sample can be neglected for this application.

For the 3D reconstruction, filtered back-projection using the FDK algorithm [41], the commercial software Xact of RX solutions was used. The voxel size of the reconstructed volume was 981 nm^3 (unchanged from the projections).

The reconstructed data with the size of $994 \times 1762 \times 269$ voxels were segmented in the industrial CT analysis software VGStudioMax3.3 from Volumegraphics using its advanced surface determination approach for single material. The algorithm determines the material boundary on the basis of the local gray value gradients taking into account the neighboring voxels. Afterwards the surfaces were converted to a triangle mesh using the grid-based (precise and watertight) preset of VGStudioMax3.3. For the mesh generation the previously determined surface definition was used applying the options “Create triangle mesh” and “Create closed surface”. For further analysis the mesh was exported to a file in STL format.

Python programming language scripts were modified to operate with the STL files (Numpy-stl library for reading), and different algorithms were implemented to extract parameters of interest [33]. The volume for each one of the peaks can be determined by integrating the volumes between the peak surface and the horizontal plane defined as base of the sample. With access to the STL raw data (vertices on the triangulated surface) any other parameter such as height, lateral surface area, axes lengths at given heights, or bottom area can be easily calculated, as well as any cross-section of the structure can be visualised. The data treatment is described in our previous publication in detail [33].

3. Results and discussion

3.1. Ion production

Figure 3(a) shows a typical mass spectrum used for the calculation of the amount of ablated and generated singly charged Ru ions. This spectrum was obtained by the accumulation of 10,000 single-pulse mass spectra in the mass range (90–110) m/z. Integration of all Ru isotope peaks gives the total number of registered electrons at the detector anode for all recorded Ru^+ ions formed at each single ablation ionization event. The derived electron number was normalized by the gain of the MCPs for the given voltage difference [37]. Figure 3(b) shows the accumulated Ru^+ signal for each applied burst count at different pulse energies. Data points for pulse energies near the ablation threshold are indicated in blue. Mass spectra recorded at a pulse energy of 0.02 µJ lack any Ru peaks indicating that this applied pulse energy is below the ablation threshold energy. In the mass spectra at 0.04 µJ and 0.09 µJ a clear Ru signal above the noise level was identified, but only after accumulation of a defined sequence of laser pulses applied on the same location, e.g., for 0.04 µJ after ~2,000 pulses and for 0.09 µJ after ~5 pulses.

Data points shown in red in Fig. 3(b) relate to pulse energies where a Ru^+ signal was observed from the very first applied laser pulse. However, for these pulse energies, the produced Ru^+ signal started out with a very low signal-to-noise ratio (SNR) and only became significant after a sequence of defined laser pulses. This particular signal behavior suggests that the surface first needs to be modified to a certain extent to enable the formation of a stable ion signal by laser ablation. The required number of laser pulses to reach the effective ion signal depends on the pulse energy.

Pulse energies in black in Fig. 3(b) were high enough to produce a strong ion signal from the first laser pulse on. By normalizing the accumulated ion intensity to the burst count, we derive the ion rate. It becomes evident that during the ablation process, the ion production rate

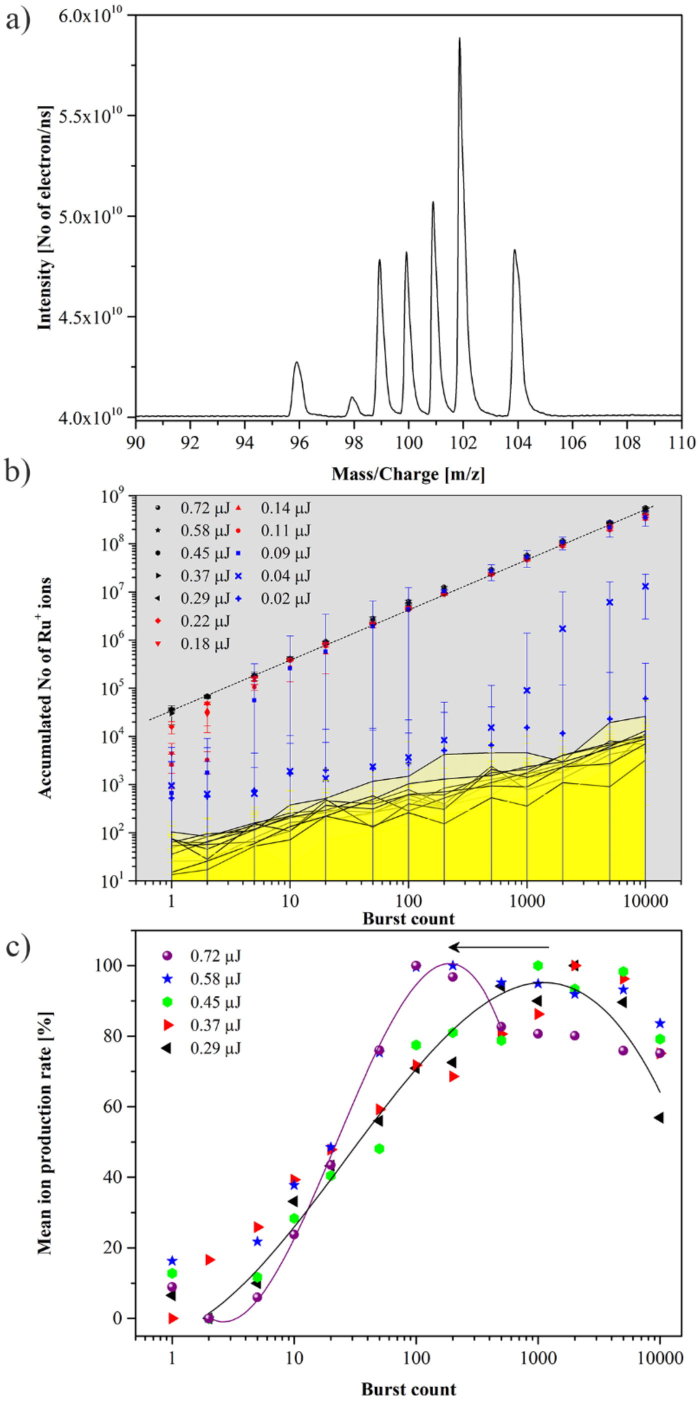

Fig. 3. a) Mass spectrum showing the mass range for all considered Ru isotopes. The spectrum is a histogram of 10’000 mass spectra recorded at a pulse energy of 0.04 µJ. b) Recorded number of Ru + ions for different applied burst counts as function of laser energy. The yellow areas in panel b illustrate the noise level. Measurements of pulse energies near the ablation threshold are indicated in blue. c) Relative number of recorded Ru + ions normalized to the applied laser burst count for the five highest pulse energies. Arrow indicates the shift of the maximum ion rate with higher pulse energies. Data points are fitted by a third order polynomial curve.

reaches a maximum which appears to be reached for lower burst rates for higher pulse energies (see Fig. 3(c)). To understand how the recorded signal is correlated to the ablation process, an in-depth analysis of the generated craters is needed, which is presented in the following sections.

3.2. Laser ablation crater analysis by SEM

A simple method to determine the ablation threshold energy is based on SEM imaging of the ablation craters.

Figure 4(a) presents SEM micrographs of craters formed at different laser settings, with the left column showing images of the entire crater area and the columns following at the right showing corresponding magnifications (5x or 20x) of selected regions of each crater area. The top row shows an area affected by one laser pulse with an energy below the threshold for the formation of ionized species. All panels below show craters formed with a pulse energy of 0.72 µJ far above the ablation and ionization threshold at 1, 10, 100, and 10,000 applied laser pulses. In this study, two distinct crater areas are identified; a rougher part located in the center of the crater (Ar), and a surrounding smoother part (As) (see white arrows top left in Fig. 4(a)).

The original sample surface is very smooth with nm roughness. Therefore, it is possible to observe irradiated zones that were only marginally modified by the laser via changes of the contrast in the SEM. The irradiated spot presented in the top micrographs of Fig. 4(a) clearly has a different appearance in the SEM images than the surrounding non-irradiated sample surface. However, it does not show the typical rough topography with protrusions and cavities at the nm-scale, which appear only after the application of multiple pulses. We observe that for a pulse energy of 0.72 µJ, it is necessary to apply 10 pulses to obtain these features (not shown in Fig. 4(a)). Also, the so-called laser-induced periodic surface structures (LIPSSs) [42–44] can be observed as a consequence of accumulated modifications in the bulk (shown in the magnified images of, e.g., the crater formed by 10,000 pulses). Such structures were reported to form upon interferences of an incident laser beam with, e.g., surface plasmon polaritons (SPPs). For pulse energies above the ablation threshold, they always occur only after irradiation with multiple pulses. Besides LIPSSs there is also a zone around the crater being affected by redeposited materials.

The lowest tested pulse energy, 0.02 µJ, did not generate any spots on the surface visible with the SEM and is therefore identified to be below the ablation damage threshold. This agrees with the mass spectrometer data, where no Ru signal was observed. Furthermore, up to 0.11 µJ, the surface does not show roughing after applying the first laser pulse, but only after the application of several consecutive laser pulses on the same location.

The number of pulses required to see a roughening of the surface correlates to the onset of the ion signal in the mass spectrometer data. For instance, at a pulse energy of 0.04 µJ, an accumulation of 2,000 single pulse mass spectra was required to identify a Ru signal above the noise level (see Fig. 3(b)). At exactly this number of applied laser pulses, a rough area started to be visible in the SEM analyses. For a pulse energy of 0.09 µJ, both observations (clear Ru signal and rough surface) required only five accumulated laser pulses.

In this respect, the rough part appears to be the actual ablation crater where crystal bond breaking, material ejection, and ionization take place. The smooth areas are zones of the modified surface where no significant ablation and ionization occurred, also referred to as affected zones. The magnified view of the rough part shows the typical protrusions and cavities at the nm-scale, which have been reported earlier for laser ablation of Cu, Pt and other metallic samples [30,45].

When the size of the rough area (Ar) for single laser pulse events is plotted as a function of the pulse energy, a trend can be observed (see Fig. 4(b)). This trend is nicely fitted by a one-sided Gaussian function, a consequence of the Gaussian beam profile, giving a peak value for crater area at around 63.1 µm^2 at 0.74 µJ. 1/e^2 of this energy (0.74 µJ) is 0.10 µJ, which is close to the ablation damage threshold energy of ~0.11 µJ derived from the correlation between D^2 (diameter

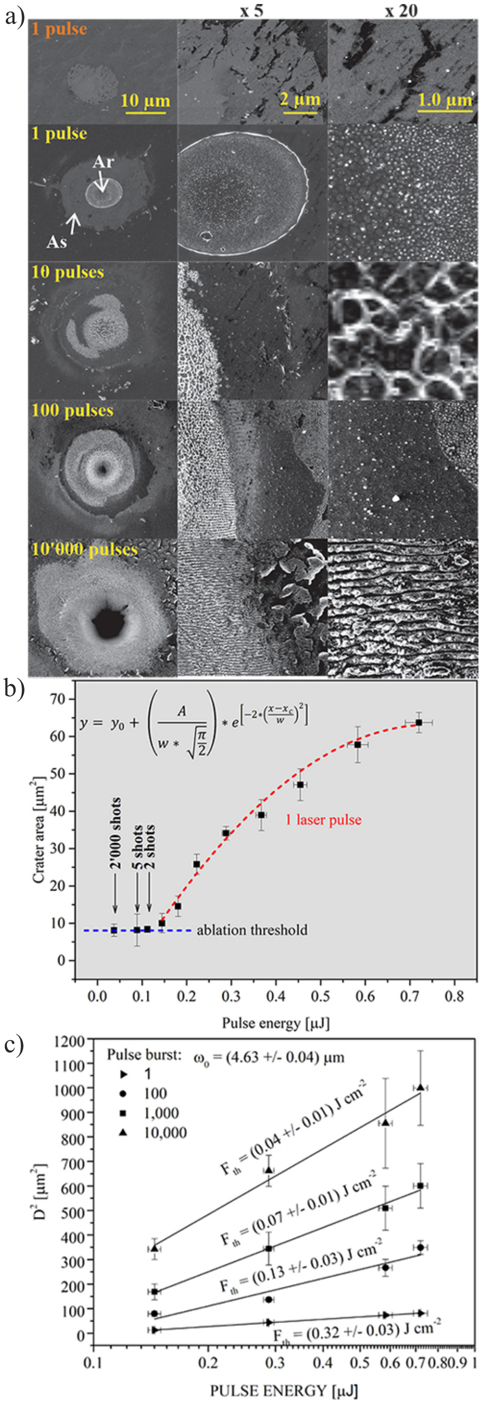

Fig. 4. a) SEM images of craters formed by 1 laser pulse at 0.04 µJ (indicated in orange), and 1, 10, 100, and 10,000 laser pulses (indicated in yellow) at a pulse energy of 0.72 µJ. b) Crater area for one laser pulse as a function of the laser pulse energy. Below a critical pulse energy craters become only visible after irradiation with multiple laser pulses. c) Linear correlation between the crater area and the logarithm of the applied pulse energy, $\ln(E_p)$. The slope of the fit for 1 single pulse gives the area of the beam waist. The intercept with the x-axis gives the threshold fluence. Considering a constant beam waist of 4.63 µm it becomes obvious that the fluence decreases with increasing burst count.

of measured rough parts of the craters) and applied pulse energy (see Fig. 4(c)) [46,47,48]. Through the slope of the fit of the one laser pulse event campaign a beam waist ω_0 of (4.63 +/- 0.04) µm can be derived. Note, ω_0 is defined as the radial distance from the beam propagation axis, where the intensity of the pulse has decreased to 1/e^2 of its maximum intensity. Knowing the beam waist ω_0 the threshold peak fluence of Ru(0001) can be derived via $F_{th} = \frac{E}{(\pi\omega_0{}^2/2)}$ with E the pulse energy. For a single laser pulse, we derived the damage threshold fluence of (0.32+/- 0.03) J cm^{-2}. The same calculation was done for larger burst counts and there it was observed that the energy level (fluence) decreases with successive laser pulses. Similar observations have been reported for other materials [47,49,50].

A possible explanation for the lowering of the ablation threshold with the number of laser pulses is that the peripheral zones of the irradiated surface area, which have not yet experienced ablation, have incurred modifications of the surface (see Fig. 4(a)) that changes the intrinsic material property with different light absorption behavior for the subsequent laser pulses promoting ablation at subsequent laser pulses. The larger the modification of the material as a result of accumulated modifications of the irradiated surface, the lower the expected ablation threshold at these zones. Consequently, the size of the ablated area will follow the spatial distribution of the Gaussian profile below the energy threshold level which initially induced the ablation of the first pulse. This would explain why pulse energies below the single pulse ablation threshold are able to ablate and ionize the material after processing the substrate with a sequence of laser pulses.

3.3. Interferometry

From SEM and mass spectrometry analysis alone, it is not clear whether the modified zones are simply not affected by material removal or if they actually underwent a material ejection but only of neutral species, which are not measured with the LIMS system. Interferometric Microscopy (IM) provides an accurate method to study the shape and volume of shallow craters with low depth to diameter ratios, similar to atomic force microscopy (AFM). IM has the advantage over AFM that it is a non-contact measurement, i.e., it does not require a physical contact with a sharp tip on a cantilever to profile the surface of the substrate. With interferometry it is possible to scan within few seconds a larger area that can comprise several craters, whereas an AFM measurement of a crater easily will last several minutes. Figure 5(a) presents IM line scans of craters formed by a single laser pulse at different pulse energies.

The shallowest measurable single pulse crater has a diameter of 3.78 µm and a depth of 17 nm, and was generated by a pulse energy of 0.14 µJ (Fig. 5(a)). Below that pulse energy no crater for a single laser pulse was detected with IM. However, for 0.09 µJ a crater formed by two-laser pulses was measurable and has a diameter of 3.49 µm and a depth of 25 nm (Fig. 5(b)). These craters have a diameter that is slightly below the one corresponding to ω_0 of a single crater.

The individual line scans of the craters generated at different pulse energies illustrate the propagation of the Gaussian profile in depth (Fig. 5(a)). A slight asymmetry in crater cross sections in Fig. 5(a) can be observed; i.e., compare the crater cross section produced at pulse energies of 0.58 µJ and 0.72 µJ. The observed asymmetry might the result of not 100% matching right angle between incident laser beam and sample surface, as well as the manual placement of the cross-hair over the crater to receive the larger axis. IM as a source of this asymmetry can be excluded with our best current knowledge. Further note, the almost perfect gaussian beam profile of the fundamental laser wavelength of 775 nm is slight distorted by the crystals of the harmonic generators as well.

Panel b in Fig. 5 presents the successive increase of the crater shape with increasing number of applied laser pulses for the same pulse energy (0.09 µJ). Note that the observed overshoots at the crater edges might be an artefact of the interferometry measurements resulting from internal reflections in the crater and might also have been altered by the baseline correction after the measurements. For this reason, they will not be further discussed in this contribution.

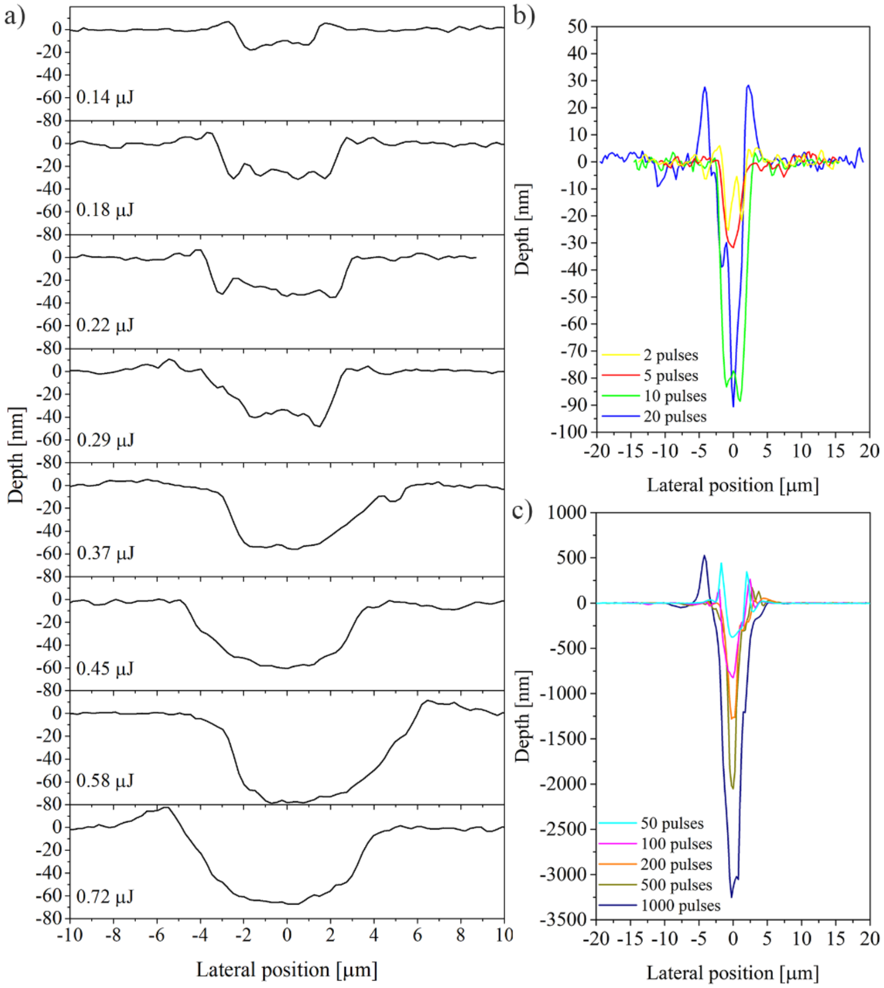

Fig. 5. Interferometry line scans. a) Depth profiles of single laser pulse craters formed at different pulse energies. b) Depth profiles of craters formed by multiple laser pulses at a pulse energy of 0.09 μJ. All profiles were baseline corrected using the moving mean with about 8 anchor points and a line interpolation.

With interferometry, it is possible to investigate the actual cavity at the irradiated spot because it allows to measure via topography the boarders of the craters. Therefore, it allows to investigate whether or not the smooth area seen in SEM is actually affected by material removal. Figure 6(a) compares the crater diameters resulting from interferometry measurements with the crater diameters determined by SEM. Cross-sectional analysis of the cavity shows that the central rough part measured in SEM forms the actual ablation crater, and no significant depressions in the surface could be identified around these locations (see Fig. 5(b)), which demonstrates that the peripheral zones of the affected areas (the smooth area) are not significantly affected by material removal.

Note that the accuracy of the crater diameter determined via cross-sectional analysis is, however, highly dependent on the geometry of the crater and can, therefore, vary on the position of the line scan. Further, only two crater repetitions were considered for the interferometry measurements, which might explain the larger error bars for the crater radius measurements in Fig. 6(a). The

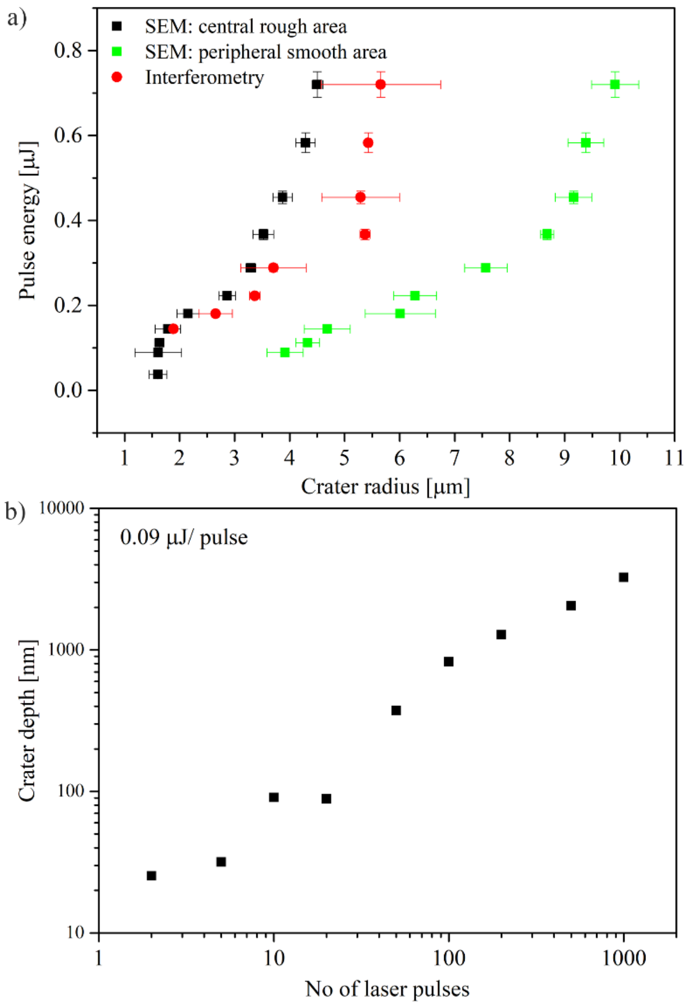

Fig. 6. a) Comparison of 1 pulse crater radius measured by interferometry (mean of two measurements) and SEM (mean of five measurements) shows that the rough area seen in the SEM is the actual crater. b) Crater depth evolution for a moderate pulse energy (0.09 µJ) with increasing number of applied laser pulses.

one-micrometer shift between the two analysis methods for the central part could be caused by the lower contrast that was obtained in the SEM for larger craters. Moreover, steeper craters were observed to form reflections on the upper sidewalls, which as well interfere with the determination of the crater size.

Figure 6(b) illustrates the evolution of the crater depth at the beginning of the ablation process for a pulse energy of 0.09 µJ. Please note that both axes are in log-scale. The graph shows that for this pulse energy, the first few laser pulses induce only moderate material ablation, i.e., after 20 pulses a layer thickness of only about 90 nm is removed. This observation goes along with the MS analysis, which indicates that for this particular pulse energy around 20 laser pulses are required to have a linear increase of Ru^+ signal with consecutive pulse numbers (see Fig. 3(b)). The subsequent linear increase of Ru^+ from 20 laser shots onwards corresponds with the rapid increase of the crater depth.

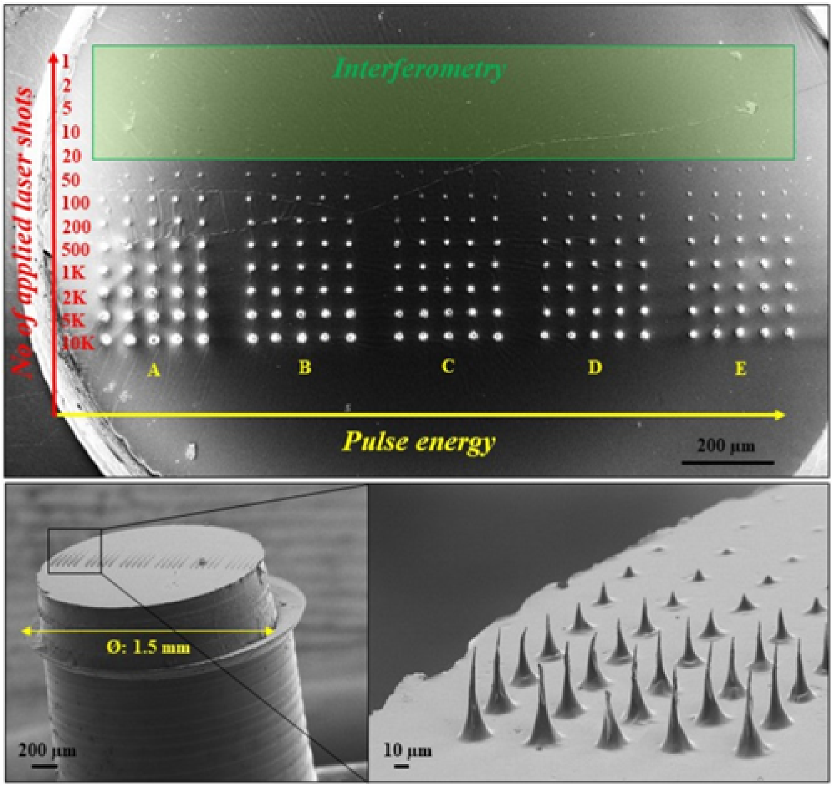

Fig. 7. SEM images of the PDMS cast in the adapted shape with limited width for the subsequent nanoCT measurement. The cast included the raster campaigns A-E, which involve the pulse energy range (0.72 - 0.29) µJ and the burst counts between 1 and 10,000. Craters formed with less than 50 laser pulses were too small to be analyzed by X-ray CT. The volumetric information of these craters was taken from interferometry.

3.4. PDMS casting and X-ray CT

While interferometry is a very convenient method to analyze the initial crater formation, it is not applicable to craters with depths larger than their diameters, to craters with rough crater sidewalls or non-planar samples that make topographical imaging impossible. As it is also important to understand the ablation evolution in larger depths (e.g., the analysis of micrometer thick layers) a different approach based on a molding procedure with a PDMS and curing agent mixture was applied on the larger craters [30]. This mold was then subjected to 3D measurement via X-ray CT. To reach sub-micrometer spatial resolution in the CT measurement, the cast needed to be confined to a 1.5 mm lateral dimension such that it can be placed and rotated in front of the X-ray tube to cover the entire flat panel detector screen [33].

The SEM images in Fig. 7 give a top and side view of the prepared cast. Due to the limited sample size for high-resolution nanoCT, only a subsection of the ablation campaign can be replicated by one single mold. As a result, the 3D analysis with nanoCT was restricted to craters with pulse energies of (0.29–0.72) µJ. The magnified image of the mold in Fig. 7 shows the real steep cone-like shape of the ablation craters and illustrates impressively how important it is to consider the full 3D geometry for an accurate determination of the crater's volume.

CT measurements of the cast allow to account for any 3D shape of the craters, which enable realistic models for the prediction of the ablation process. Figure 8 presents a nanoCT image

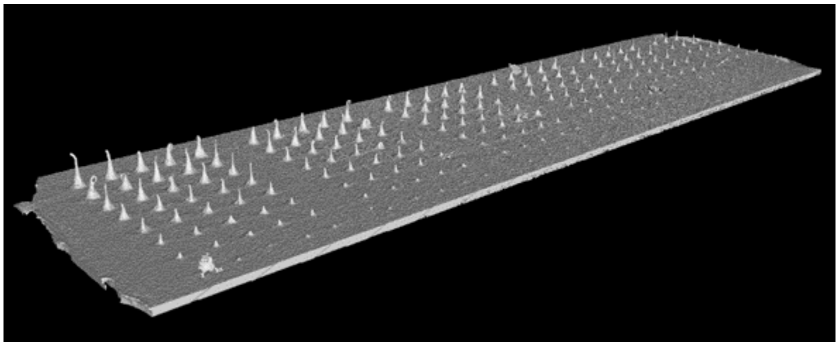

Fig. 8. CT image of the PDMS cast after surface reconstruction and PDMS-air interface determination showing the relevant region of interest.

of the PDMS cast after surface determination. The dimensions of the craters formed with less than 50 laser pulses were below the resolving power of the CT measurement (<500 nm). The 3D information of these craters was therefore acquired via interferometry.

Figure 9(a) shows the dependence of the ablation depth on the applied number of laser pulses for the craters formed in the pulse energy range of (0.72–0.29) µJ (raster A–E, see Fig. 1). The depth of the craters increases continuously with the number of applied laser pulses up to a certain point which depends on the pulse energy. Beyond this point, the curve flattens and only a very moderate increase of the ablation depth with every additional laser pulse is observed, resulting in a maximum depth of about (20–35) µm. The maximum depth (derived by an asymptotic function) is a function of the irradiance (Fig. 9(b)), which is the energy of the pulse over the initial single pulse crater area (Fig. 4(a)) for that energy and the pulse width (~170 fs after high-harmonic generation of the UV pulses). This crater depth evolution indicates that the maximum achievable depth is not limited by the Rayleigh range of the laser focus $z_R = \frac{\pi {\omega_0}^2}{\lambda}$, as this would amount to z_R~261 µm for a ω_0 of 4.63 µm and a λ of 258 nm. Förster *et al.* reported that the ablation of a sample surface with laser pulses of Gaussian spatial and temporal profiles will always generate craters of a certain maximum aspect ratio, whereas this aspect ratio depends on the applied laser power, the material-specific ablation threshold, and the beamwidth [51]. They describe that upon progressive crater depth a dilution of the applied laser fluence occurs, which comes from the homogenous distribution of the incident pulse energy upon multiple reflections on the crater sidewalls. In this way, the effective irradiated area is the surface area of the crater walls, which increases upon progressing crater depth. The ablation process comes to an end when the ablation fluence reaches the ablation threshold of the corresponding material [51], which we observe also in our measurements, as discussed below.

When plotting the crater volume against the crater depth for all number of laser pulses (Fig. 10(a)), we find that there are two regions that depend on the crater volume and depth, namely a linear region and a quadratic region. Information on the volume and depth for all craters up to 20 laser pulses were obtained from interferometry measurements, whereas all the others were obtained from CT. The linear growth of the crater volume with depth consistently holds true up to a depth of about 10 µm, which corresponds to between 200 and 1,000 applied laser pulses, depending on the pulse energy. Therefore, the change of correlation is not an artefact related to the different measurement techniques. Above approx. 10 µm depth, the volume grows quadratically with increasing depth. Panel 10b plots the ablation rate, which is defined here as the ablated volume normalized by the applied laser burst, against the ablated depth for two pulse energies. In this representation, three distinct regions can be observed. The first regime, the initial crater formation, shows a decreasing ablation rate that lasts until a depth of about 0.4 µm

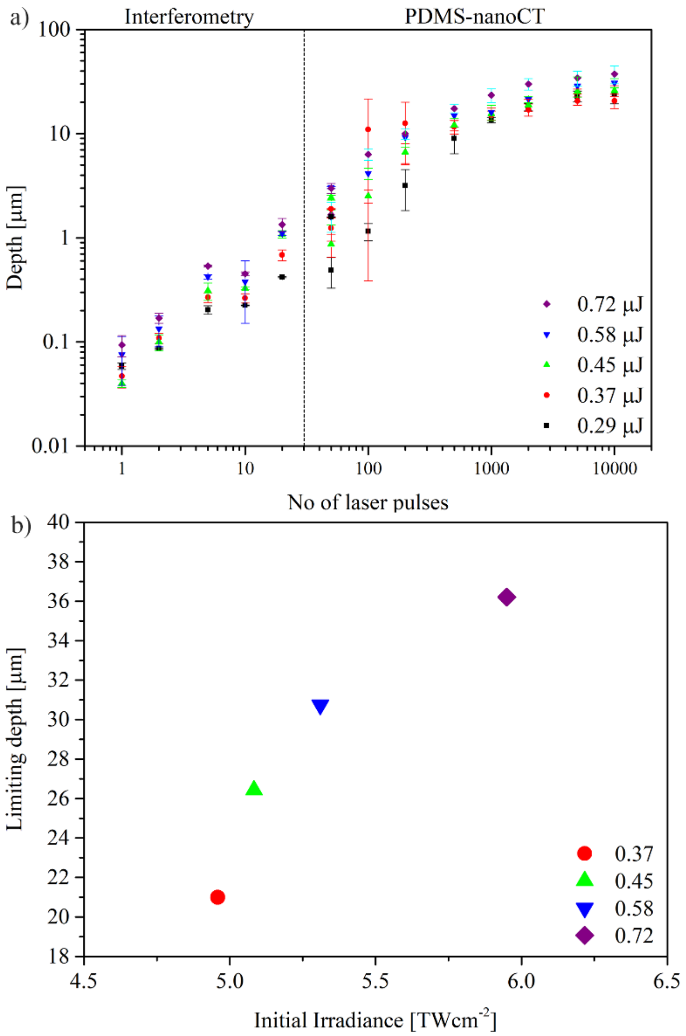

Fig. 9. a) Crater depths as a function of the applied number of laser pulses for five different pulse energies. Each data point is a mean of five craters formed at distinct locations. b) Correlation of expected maximal depth derived by an asymptotic function, and irradiance.

and requires for 0.29 μJ pulse energy the application of 20 to 50 pulses and for 0.72 μJ pulse energy about 10 pulses. The second regime, the linear crater growth, shows a more constant ablation rate that holds steady to a depth of 10 to 20 μm and requires up to 1,000 pulses for 0.29 μJ, and up to 500 for 0.72 μJ. In the third regime, reaching the depth limit, the ablation rate is decreasing exponentially, which is observed above 1,000 laser pulses for 0.29 μJ and above 500 laser pulses for 0.72 μJ.

The transition to the third regime is probably related to reaching the threshold ablation fluence on the crater walls $F_{th} = (0.32 +/- 0.03)$ J cm^{-2}, as discussed above. In Fig. 10, panel c, we plot the effective fluence that is the pulse energy (E_p) divided by the area of the crater sidewall (A_{SW}). When the crater becomes too large, the pulse energy is spread out over the large area of the sidewalls and can no longer effectively ablate material in the depth. Reaching this limit is observed by a sudden strong decrease in the ablation rate in the case of both pulse energies. If the ablation process completely stops from this point on, one would assume a drastic drop of the

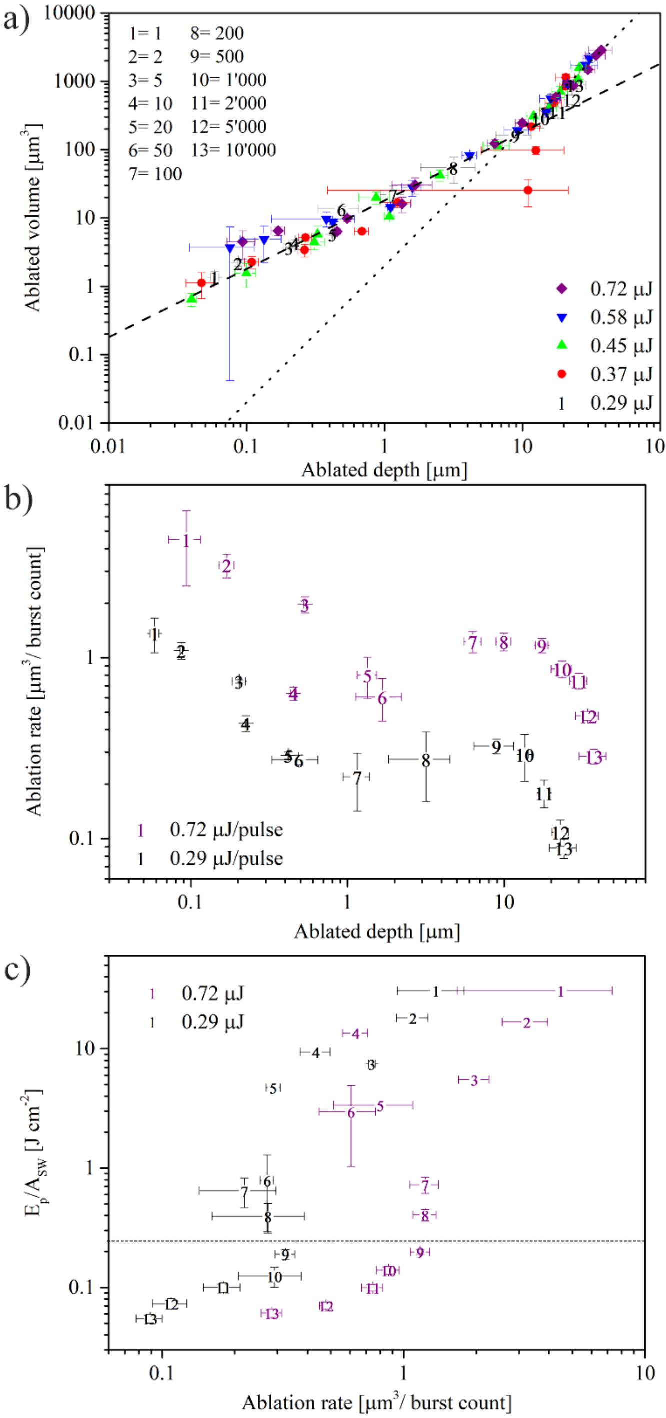

Fig. 10. a) Ablated volume versus ablated depth. The correlation from linear to quadratic changes at about 10 µm depth. b) Progression of ablation rate based on ablated volume, with ablated depth, shows three distinct regimes. c) Ablation flux, i.e., the ratio of the applied pulse energy, E_P, and the crater sidewall area, A_{SW}, as function of the ablation rate. The plotted numbers in all three panels indicate the burst count for the corresponding data point (see legend in a) and Fig. 1).

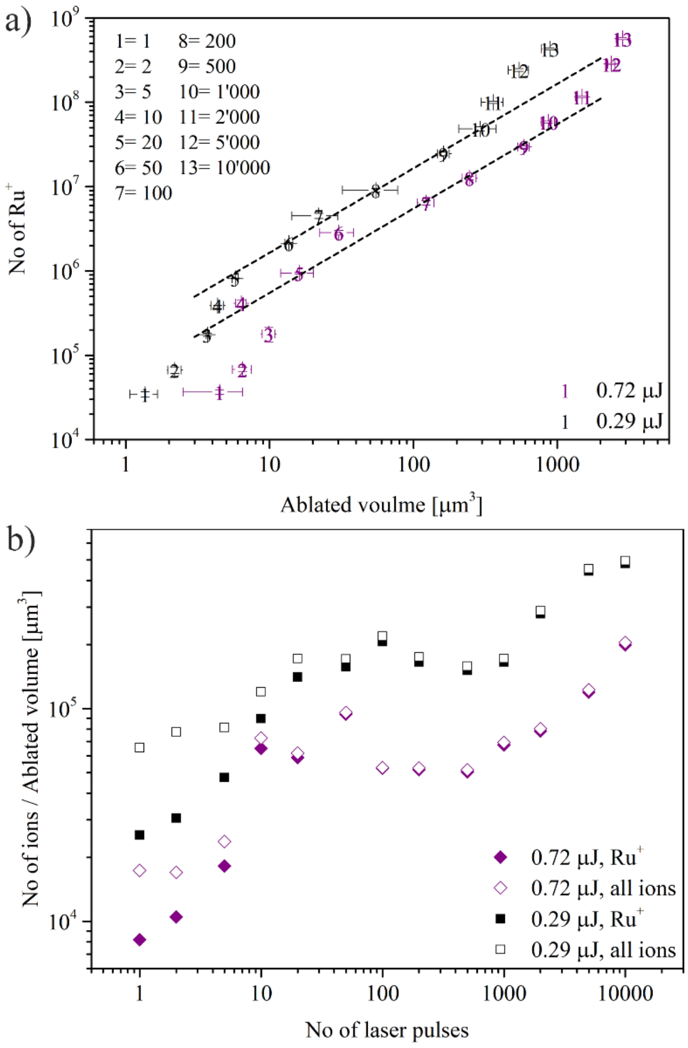

Fig. 11. a) Accumulated number of detected Ru + ions as function of the measured ablated crater volume for selected pulse energies. b) Ionization rate as accumulated number of recorded ions normalized by the ablated volume, for each applied burst count. The correlation plot shows three different regimes. Between 0.4 µm and 10–20 µm crater depth a stable ablation and ionization rate is observed.

ion signal, which however was not observed. Instead, for the subsequent laser pulses, the ratio between the Ru^+ signal and the ablated volume even became slightly larger (Fig. 11(a)).

Figure 11(a) shows the ion signal measured as function of the crater volume ablated. In the second regime, the linear crater growth, there is a linear correlation of the amount of generated ions and ablated volume with the pulse numbers assigned (10–2,000 for 0.72 µJ/pulse, 50–1,000 for 0.29 µJ/pulse). Below, the initial crater formation, and above, reaching the depth limit, a non-linear correlation is found.

The relative increase of Ru^+ ions in the last regime exceeding the increase in ablated volume implies that the ionization efficiency improves. A possible explanation for this behavior could be related to an increase in the plasma temperature upon a sudden change of the ablation conditions. The plasma plume has already been reported to have an erosive effect on the surrounding material, particularly in deeper craters, where the plasma gets spatially confined [52]. Additionally, we expect that upon irradiation defects in the crystal structure are formed all around the crater borders, because each pulse acts uniformly on the crater bottom and sidewalls. This so-called affected zone is continuously ablated and reformed during the ablation process. However, at a certain depth, when the laser fluence drops to the ablation threshold, this affected zone with altered material property and better light absorption characteristics may become the only source for ablation. The small aperture at the crater bottom, which confines the spreading of the plasma plume in deeper layers, could be the reason for higher plasma temperatures that generate more ionized species even though the overall ablation rate decreases. Since the affected zone is distributed all around the crater the continuation of the ablation promotes the growth of the crater along the sidewalls, which can explain the change to the quadratic correlation of the ablation volume and ablation depth in Fig. 10(a).

The non-linear ablation behavior at the surface might be of a different nature than in the bulk. Figure 11(b) compares the fraction of Ru^+ ion with the total number of recorded ions in the ablated volume for a different number of laser pulses. The graph shows that, initially, the ablation plume consists to a large extent of other ions which might originate from an impurity layer (e.g. oxide) on the surface. The number of laser pulses needed to remove this impurity layer and to obtain an ablation plume consisting mainly of Ru^+ ions ranges from about 50 for 0.29 µJ to 10 for 0.72 µJ, which matches the number of laser pulses required to reach the linear correlation between the Ru^+ signal and the ablated volume in Fig. 11(a), and the number of laser pulses required to reach ~0.4 µm depth in Fig. 10(b). Beyond the first 0.4 µm until about 10 µm (1,000 and 2,000 pulses for 0.29 and 0.72 µJ, respectively), which corresponds to the linear regime, the number of Ru^+ ions produced per ablated volume is constant.

The comparison of the two pulse energies (0.29 µJ and 0.72 µJ) in Fig. 11 also demonstrates that the ionization and the ablation process are two independent processes. More than doubling of the pulse energy enhances the ablation rate. However, the number of ionized species does not increase proportionally.

4. Conclusions

A detailed study on UV-fs laser ablation was performed on a Ru single crystal. A combination of SEM, interferometry, X-ray computed tomography, and mass spectrometry are used to reveal important aspects of the laser and the ablation process, such as the beam waist, the ablation threshold, the formation of affected zones, the ablation profile, the ablation rate, and the maximum achievable ablation depth for the specific instrument settings.

The study consisted of the formation of various types of ablation craters, each one created under different irradiation conditions that involved combinations of different pulse energies (0.02–0.72 µJ) and laser burst counts (1–10’000), resulting in crater depths ranging from <20 nm to ~40 µm. A single crystal substrate was chosen to minimize possible location variations and simplify the comparison of different ablation parameters.

SEM was used to investigate the ablation threshold and laser beam waist, which were found to be ~ 0.3 J cm^{-2} and 4.63 µm. The high contrast in SEM allowed to identify two different regions at the irradiated surface; a central, rough part containing nanometer-sized protrusions and cavities, and a smooth peripheral part.

Linking mass spectrometry and interferometry analysis to the SEM results revealed that the appearance of nanometer features on the irradiated surface goes along with the onset of the ion signal from the substrate. Further, cross-sectional line scans of the craters showed no significant depression in the peripheral zones, even though they exhibit a different contrast than the not irradiated surface. These smooth parts were observed to appear in the center of the irradiated surface, before the formation of the cavity and the measurement of any ionized species. These parts might be a sort of affected zone with defects in the crystal structure that may affect the absorption of laser light for the subsequent pulses.

The 3D analysis of the PDMS-molded crater's negatives applying the novel X-ray tomography methodology revealed new insights into the ablation process that are relevant for chemical depth profiles. A linear correlation between the crater volume and the crater depth could be identified, which was maintained to a specific depth and depends on the pulse energy, before turning to a quadratic correlation. Our results are in line with previous studies on picosecond laser pulses which predict a limiting crater depth as a function of beam waist, applied laser fluence, and material-specific ablation threshold. The limiting depth is a consequence of homogenously distributed fluence along the crater sidewalls, which decreases with progressing ablation, up to the point where the ablation threshold is reached on the crater walls.

The detailed analysis of the generated laser ablation craters via X-ray CT imaging in combination with the PDMS imprint approach represents a high light in this study and a complementary extension of conventional laser ablation characterization techniques. The method allows the characterization of a complete array of various ablation craters with different shapes and dimensions in one step, allows for very large aspect ratio features, with sub-micrometer accuracy, and is independent of the actual material in which the craters have been produced. Additionally, in comparison to other imaging techniques, such as AFM or the IM used in this study, the X-ray CT imaging method is not limited to aspect ratios of the craters, providing information that is otherwise missing, with a similar or even better resolution. Consequently, spatially resolved chemical analysis of complex materials using laser ablation-based techniques, such as LA-ICP-MS, LIBS, and LIMS, can be calibrated efficiently and accurately at the same time, and therefore allows to provide high accurate chemical information of the material investigated. While X-ray CT can be performed in principle directly on typical laser-ablation specimens in case of high-energy cyclotron radiation [53], the X-ray CT of PDMS replicas can be handled with lab-based X-ray scanners, operating at lower energies and resolution. Here, PDMS still provides enough contrast for high-resolution X-ray imaging and its molding can be done on any material making it a very versatile and generic approach.

Complementing the 3D analysis with mass spectrometric measurements of the Ru^+ signal further showed that the entire depth profile could be divided into three regimes. The first regime was related to the initial crater formation and the presence of an impurity layer (or oxide layer), which involved the first ~0.4 µm of the sample. The second regime was characterized by a stable ablation and ionization rate that extended to about 10 and 20 µm depth depending on the applied pulse energy. The third regime was characterized by a decreasing ablation rate, which, in contrast, induced a relative increase of the ion yield. At these depths the ablation process becomes less efficient, however, the ablation plume characteristic changes providing more ionization.

It is expected that the introduction of defects in the crystal structure upon irradiation does not only occur at the beginning when the crater is formed but also over the entire ablation process. This generates affected material that is distributed all around the crater walls. As described above, defects in the crystal structure change the absorptivity of the light. After achieving the limiting depth, the ablation predominantly occurs at these affected zones which, for the next couple of pulses, enlarges the crater in the lateral direction and increases the ion count relative to the ablated volume.

Because the ablation and ionization are kept at a constant rate in the second regime, it is possible to derive the crater depth during the measurement by following the ion signal of the substrate. Before that regime, crater formation effects and the measurement of impurity layers dominate the chemical analysis. After this regime, the contribution of material from the sidewalls becomes more important, and increased mixing of different layers is expected. Therefore, this new measurement approach is of importance for future chemical depth profiling studies, analyzing e.g., complex layered structures used in the semiconductor industry where e.g., chemical information is important to be linked to a certain location in the material of interest.

Funding. Schweizerischer Nationalfonds zur Förderung der Wissenschaftlichen Forschung (200020_149224, 200020_172507, 51NF40 182895, P2BEP2_165378).

Acknowledgments. We acknowledge the work from the technical staff of the department of Chemistry, Biochemistry and Pharmaceutical sciences and the Space Research and Planetary Sciences division at the University of Bern, Switzerland as well as the technical (U. Drechsler) and permanent research staff (H. Wolf) at IBM Research Europe – Zurich. Additionally, this study was performed with the support of the interfaculty Microscopy Imaging Centre (MIC) of the University of Bern, Switzerland.

Disclosures. The authors declare no conflicts of interest.

Data availability. Data underlying the results presented in this paper are not publicly available at this time but may be obtained from the authors upon reasonable request.

References

1. P. Kafalas, J. I. Masters, and E. M. E. Murray, "Photosensitive Liquid used as a Nondestructive Passive Q-Switch in a Ruby Laser," J. Appl. Phys. **35**(8), 2349–2350 (1964).
2. R. E. Russo, X. Mao, H. Liu, J. Gonzalez, and S. S. Mao, "Laser ablation in analytical chemistry—a review," Talanta **57**(3), 425–451 (2002).
3. E. Bernal, L. P. Levine, and J. F. Ready, "Time-of-Flight Spectrometer for Laser Surface Interaction Studies," Rev. Sci. Instrum. **37**(7), 938–941 (1966).
4. N. C. Fenner and N. R. Daly, "Laser Used for Mass Analysis," Rev. Sci. Instrum. **37**(8), 1068–1070 (1966).
5. F. Hillenkamp, E. Unsöld, R. Kaufmann, and R. Nitsche, "A high-sensitivity laser microprobe mass analyzer," Appl. Phys. **8**(4), 341–348 (1975).
6. M. Karas and F. Hillenkamp, "Laser desorption ionization of proteins with molecular masses exceeding 10,000 daltons," Anal. Chem. **60**(20), 2299–2301 (1988).
7. J. Pisonero, B. Fernandez, and D. Gunther, "Critical revision of GD-MS, LA-ICP-MS and SIMS as inorganic mass spectrometric techniques for direct solid analysis," J. Anal. At. Spectrom. **24**(9), 1145–1160 (2009).
8. A. Limbeck, P. Galler, M. Bonta, G. Bauer, W. Nischkauer, and F. Vanhaecke, "Recent advances in quantitative LA-ICP-MS analysis: challenges and solutions in the life sciences and environmental chemistry," Anal. Bioanal. Chem. **407**(22), 6593–6617 (2015).
9. J. Laserna, J. M. Vadillo, and P. Purohit, "Laser-Induced Breakdown Spectroscopy (LIBS): Fast, Effective, and Agile Leading Edge Analytical Technology," Appl. Spectrosc. **72**(1_suppl), 35–50 (2018).
10. J. J. Gonzalez, "Laser Ablation-Based Chemical Analysis Techniques: A Short Review," Spectroscopy **32**, 28–34 (2017).
11. F. Scott Anderson, J. Levine, and T. J. Whitaker, "Rb-Sr resonance ionization geochronology of the Duluth Gabbro: A proof of concept for in situ dating on the Moon," Rapid Commun. Mass Spectrom. **29**(16), 1457–1464 (2015).
12. R. Wiesendanger, D. Wacey, M. Tulej, A. Neubeck, M. Ivarsson, V. Grimaudo, P. Moreno-García, A. Cedeño-López, A. Riedo, and P. Wurz, "Chemical and Optical Identification of Micrometer-Sized 1.9 Billion-Year-Old Fossils by Combining a Miniature Laser Ablation Ionization Mass Spectrometry System with an Optical Microscope," Astrobiology **18**(8), 1071–1080 (2018).
13. S. Frey, R. Wiesendanger, M. Tulej, M. Neuland, A. Riedo, V. Grimaudo, P. Moreno-García, A. C. López, M. Mohos, B. Hofmann, K. Mezger, P. Broekmann, and P. Wurz, "Chemical analysis of a lunar meteorite by laser ablation mass spectrometry," Planet. Space Sci. **182**, 104816 (2020).
14. C. J. Kelly, C. R. M. McFarlane, D. A. Schneider, and S. E. Jackson, "Dating Micrometre-Thin Rims Using a LA-ICP-MS Depth Profiling Technique on Zircon from an Archaean Metasediment: Comparison with the SIMS Depth Profiling Method," Geostand. Geoanal. Res. **38**(4), 389–407 (2014).
15. V. Grimaudo, P. Moreno-García, A. Riedo, S. Meyer, M. Tulej, M. B. Neuland, M. Mohos, C. Gütz, S. R. Waldvogel, P. Wurz, and P. Broekmann, "Toward Three-Dimensional Chemical Imaging of Ternary Cu–Sn–Pb Alloys Using Femtosecond Laser Ablation/Ionization Mass Spectrometry," Anal. Chem. **89**(3), 1632–1641 (2017).
16. M. Tulej, A. Neubeck, M. Ivarsson, A. Riedo, M. B. Neuland, S. Meyer, and P. Wurz, "Chemical Composition of Micrometer-Sized Filaments in an Aragonite Host by a Miniature Laser Ablation/Ionization Mass Spectrometer," Astrobiology **15**(8), 669–682 (2015).
17. V. A. Azov, L. Mueller, and A. A. Makarov, "LASER IONIZATION MASS SPECTROMETRY AT 55: QUO VADIS?" Mass Spectrom. Rev. **41**(1), 100–151 (2022).
18. R. E. Russo, X. Mao, J. J. Gonzalez, and S. S. Mao, "Femtosecond laser ablation ICP-MS," J. Anal. At. Spectrom. **17**(9), 1072–1075 (2002).
19. B. Zhang, M. He, W. Hang, and B. Huang, "Minimizing Matrix Effect by Femtosecond Laser Ablation and Ionization in Elemental Determination," Anal. Chem. **85**(9), 4507–4511 (2013).
20. A. Riedo, M. Neuland, S. Meyer, M. Tulej, and P. Wurz, "Coupling of LMS with a fs-laser ablation ion source: elemental and isotope composition measurements," J. Anal. At. Spectrom. **28**(8), 1256–1269 (2013).

21. D. Käser, L. Hendriks, J. Koch, and D. Günther, "Depth profile analyses with sub 100-nm depth resolution of a metal thin film by femtosecond - laser ablation - inductively coupled plasma - time-of-flight mass spectrometry," Spectrochim. Acta, Part B **149**, 176–183 (2018).
22. M. Dong, L. Wei, J. J. González, D. Oropeza, J. Chirinos, X. Mao, J. Lu, and R. E. Russo, "Coal Discrimination Analysis Using Tandem Laser-Induced Breakdown Spectroscopy and Laser Ablation Inductively Coupled Plasma Time-of-Flight Mass Spectrometry," Anal. Chem. **92**(10), 7003–7010 (2020).
23. V. Grimaudo, M. Tulej, A. Riedo, R. Lukmanov, N. F. W. Ligterink, C. de Koning, and P. Wurz, "UV post-ionization laser ablation ionization mass spectrometry for improved nm-depth profiling resolution on Cr/Ni reference standard," Rapid Commun. Mass Spectrom. **34**, e8803 (2020).
24. D. J. Hwang, H. Jeon, C. P. Grigoropoulos, J. Yoo, and R. E. Russo, "Femtosecond laser ablation induced plasma characteristics from submicron craters in thin metal film," Appl. Phys. Lett. **91**(25), 251118 (2007).
25. J. J. Gonzalez, A. Fernandez, D. Oropeza, X. Mao, and R. E. Russo, "Femtosecond laser ablation: Experimental study of the repetition rate influence on inductively coupled plasma mass spectrometry performance," Spectrochim. Acta, Part B **63**(2), 277–286 (2008).
26. J.-H. Choi, Y. Moon, S.-H. Lee, J.-H. In, and S. Jeong, "Wavelength dependence of the ablation characteristics of Cu (In, Ga) Se2 solar cell films and its effects on laser induced breakdown spectroscopy analysis," Int. J. of Precis. Eng. and Manuf.-Green Tech. **3**(2), 167–171 (2016).
27. O. V. Borisov, X. Mao, and R. E. Russo, "Effects of crater development on fractionation and signal intensity during laser ablation inductively coupled plasma mass spectrometry," Spectrochim. Acta, Part B **55**(11), 1693–1704 (2000).
28. S. Döring, S. Richter, S. Nolte, and A. Tünnermann, "In situ imaging of hole shape evolution in ultrashort pulse laser drilling," Opt. Express **18**(19), 20395–20400 (2010).
29. S. Döring, J. Szilagyi, S. Richter, F. Zimmermann, M. Richardson, A. Tünnermann, and S. Nolte, "Evolution of hole shape and size during short and ultrashort pulse laser deep drilling," Opt. Express **20**(24), 27147–27154 (2012).
30. V. Grimaudo, P. Moreno-García, A. C. López, A. Riedo, R. Wiesendanger, M. Tulej, C. Gruber, E. Lörtscher, P. Wurz, and P. Broekmann, "Combining Anisotropic Etching and PDMS Casting for Three-Dimensional Analysis of Laser Ablation Processes," Anal. Chem. **90**(4), 2692–2700 (2018).
31. P. Moreno-García, V. Grimaudo, A. Riedo, A. Cedeño López, R. Wiesendanger, M. Tulej, C. Gruber, E. Lörtscher, P. Wurz, and P. Broekmann, "Insights into Laser Ablation Processes of Heterogeneous Samples: Toward Analysis of Through-Silicon-Vias," Anal. Chem. **90**(11), 6666–6674 (2018).
32. V. Grimaudo, P. Moreno-García, A. Cedeño López, A. Riedo, R. Wiesendanger, M. Tulej, C. Gruber, E. Lörtscher, P. Wurz, and P. Broekmann, "Depth Profiling and Cross-Sectional Laser Ablation Ionization Mass Spectrometry Studies of Through-Silicon-Vias," Anal. Chem. **90**(8), 5179–5186 (2018).
33. D. Monserrat Lopez, V. Grimaudo, G. Prone, A. Flisch, A. Riedo, R. Zboray, T. Lüthi, M. Mayor, M. Fussenegger, P. Broekmann, P. Wurz, and E. Lörtscher, "Automated, 3-D and Sub-Micron Accurate Ablation-Volume Determination by Inverse Molding and X-Ray Computed Tomography," Adv. Sci. **9**(20), 2200136 (2022).
34. C. E. Mercer, P. Anderson, and G. R. Davis, "Sequential 3D X-ray microtomographic measurement of enamel and dentine ablation by an Er:YAG laser," Br. Dent. J. **194**(2), 99–104 (2003).
35. A. H. Galmed, A. du Plessis, S. G. le Roux, E. Hartnick, H. Von Bergmann, and M. Maaza, "Three dimensional characterization of laser ablation craters using high resolution X-ray computed tomography," Spectrochim. Acta, Part B **139**, 75–82 (2018).
36. A. Riedo, A. Bieler, M. Neuland, M. Tulej, and P. Wurz, "Performance evaluation of a miniature laser ablation time-of-flight mass spectrometer designed for in situ investigations in planetary space research," J. Mass Spectrom. **48**(1), 1–15 (2013).
37. A. Riedo, M. Tulej, U. Rohner, and P. Wurz, "High-speed microstrip multi-anode multichannel plate detector system," Rev. Sci. Instrum. **88**(4), 045114 (2017).
38. P. Wurz, M. Tulej, A. Riedo, V. Grimaudo, R. Lukmanov, and N. Thomas, "Investigation of the Surface Composition by Laser Ablation/Ionization Mass Spectrometry," in *2021 IEEE Aerospace Conference (50100)*, (2021), 1–15.
39. S. Meyer, A. Riedo, M. B. Neuland, M. Tulej, and P. Wurz, "Fully automatic and precise data analysis developed for time-of-flight mass spectrometry," J. Mass Spectrom. **52**(9), 580–590 (2017).
40. D. Nečas and P. Klapetek, "Gwyddion: an open-source software for SPM data analysis," Cent. Eur. J. Phys. **10**, 181–188 (2012).
41. L. A. Feldkamp, L. C. Davis, and J. W. Kress, "Practical cone-beam algorithm," J. Opt. Soc. Am. A **1**(6), 612–619 (1984).
42. F. Costache, S. Kouteva-Arguirova, and J. Reif, "Sub–damage–threshold femtosecond laser ablation from crystalline Si: surface nanostructures and phase transformation," Appl. Phys. A **79**(4-6), 1429–1432 (2004).
43. J. Bonse, A. Rosenfeld, and J. Krüger, "On the role of surface plasmon polaritons in the formation of laser-induced periodic surface structures upon irradiation of silicon by femtosecond-laser pulses," J. Appl. Phys. **106**(10), 104910 (2009).
44. M. J. Abere, M. Zhong, J. Krüger, and J. Bonse, "Ultrafast laser-induced morphological transformations," MRS Bull. **41**(12), 969–974 (2016).
45. A. Y. Vorobyev, V. S. Makin, and C. Guo, "Periodic ordering of random surface nanostructures induced by femtosecond laser pulses on metals," J. Appl. Phys. **101**(3), 034903 (2007).
46. J. M. Liu, "Simple technique for measurements of pulsed Gaussian-beam spot sizes," Opt. Lett. **7**(5), 196–198 (1982).

Optics EXPRESS

47. G. Raciukaitis, M. Brikas, P. Gecys, and M. Gedvilas, *Accumulation effects in laser ablation of metals with high-repetition-rate lasers*, High-Power Laser Ablation 2008 (SPIE, 2008), Vol. 7005.
48. S. Martin, A. Hertwig, M. Lenzner, J. Krüger, and W. Kautek, “Spot-size dependence of the ablation threshold in dielectrics for femtosecond laser pulses,” Appl. Phys. A **77**(7), 883–884 (2003).
49. M. Lenzner, F. Krausz, J. Krüger, and W. Kautek, “Photoablation with sub-10 fs laser pulses,” Appl. Surf. Sci. **154**, 11–16 (2000).
50. R. Baerbel, S. I. Dmitriy, E. G. Martin, and I. A. Sergei, “Modelling ultrafast laser ablation,” J. Phys. D: Appl. Phys. **50**, 193001 (2017).
51. D. J. Förster, R. Weber, D. Holder, and T. Graf, “Estimation of the depth limit for percussion drilling with picosecond laser pulses,” Opt. Express **26**(9), 11546–11552 (2018).
52. S. M. Klimentov, T. V. Kononenko, P. A. Pivovarov, S. V. Garnov, V. I. Konov, A. M. Prokhorov, D. Breitling, and F. Dausinger, “The role of plasma in ablation of materials by ultrashort laser pulses,” Quantum Electron. **31**(5), 378–382 (2001).
53. F.-X. d’Abzac, C. Noiriel, A. Marquet, and S. Brichau, “Comparison of 1030 nm and 257 nm wavelengths for U-Pb zircon dating by femtosecond laser ablation – Inductively coupled plasma mass spectrometry with support of 3D crater imaging,” Spectrochim. Acta, Part B **168**, 105863 (2020).